SWIFT BAT SURVEY OF AGN

J. TUELLER[1], R. F. MUSHOTZKY[1], S. BARTHELMY[1], J. K. CANNIZZO[1,2], N. GEHRELS[1], C. B. MARKWARDT[1,3], G. K. SKINNER[1,3], L. M. WINTER[1,3]

Draft version March 26, 2008

ABSTRACT

We present the results[1] of the analysis of the first 9 months of data of the *Swift* BAT survey of AGN in the $14-195$ keV band. Using archival X-ray data or follow-up *Swift* XRT observations, we have identified 129 (103 AGN) of 130 objects detected at $|b| > 15°$ and with significance $> 4.8\sigma$. One source remains unidentified. These same X-ray data have allowed measurement of the X-ray properties of the objects. We fit a power law to the $\log N - \log S$ distribution, and find the slope to be 1.42 ± 0.14. Characterizing the differential luminosity function data as a broken power law, we find a break luminosity $\log L_*$(erg s^{-1})$= 43.85 \pm 0.26$, a low luminosity power law slope $a = 0.84^{+0.16}_{-0.22}$, and a high luminosity power law slope $b = 2.55^{+0.43}_{-0.30}$, similar to the values that have been reported based on *INTEGRAL* data. We obtain a mean photon index 1.98 in the $14-195$ keV band, with an *rms* spread of 0.27. Integration of our luminosity function gives a local volume density of AGN above 10^{41} erg s^{-1} of 2.4×10^{-3} Mpc^{-3}, which is about 10% of the total luminous local galaxy density above $M_* = -19.75$. We have obtained X-ray spectra from the literature and from *Swift* XRT follow-up observations. These show that the distribution of $\log\, n_H$ is essentially flat from $n_H = 10^{20}$ cm^{-2} to 10^{24} cm^{-2}, with 50% of the objects having column densities of less than 10^{22} cm^{-2}. BAT Seyfert galaxies have a median redshift of 0.03, a maximum log luminosity of 45.1, and approximately half have $\log n_H > 22$.

Subject headings: galaxies: active — gamma rays: observations — surveys

1. INTRODUCTION

It is now realized that most of the AGN in the Universe have high column densities of absorbing material in our line of sight, which significantly changes their apparent properties across much of the electromagnetic spectrum. In many well studied objects this material significantly reduces the soft X-ray, optical, and UV signatures of an active nucleus essentially "hiding" the object. While it is commonly believed that extinction-corrected [OIII] can be used as an "unbiased" tracer of AGN activity (Risaliti et al. 1999), there is a large scatter between [OIII] and $2-10$ keV X-ray flux (Heckman et al. 2005) and between [OIII] and BAT flux (Meléndez et al 2008). We acknowledge that some Compton thick AGN are detected in [OIII] that cannot be detected in hard X-rays, but Compton thick AGN are outside the scope of this paper. Therefore, surveys of AGN which rely primarily on rest frame optical and UV studies are very incomplete and have led to misleading results concerning the number, luminosity function, and evolution of active galaxies (e.g., Barger et al. 2005).

While the distribution of column densities is under intensive investigation, it is clear from both X-ray (Tozzi et al. 2006, Cappi et al. 2006) and IR data (Alonso-Herrero, et al. 2006) that a large fraction of AGN have column densities greater than 3×10^{22} cm^{-2} in the line of sight. Using the galactic reddening law (Predehl & Schmitt 1995), this is equivalent to $A_V > 13$, making the nuclei essentially invisible in the optical and UV bands. This effect seems to dominate the population seen in deep X-ray surveys (e.g., Barger et al. 2005, Brandt & Hasinger 2005) where a large fraction of the X-ray selected objects do not have optical counterparts with classical AGN signatures.

There are only two spectral bands in which the nuclear emission is strong and where, provided the column densities are less than 1.5×10^{24} cm^{-2} (Compton-thin objects), this obscuring material is relatively optically thin. These bands, the hard X-ray ($E > 20$ keV) and the IR ($5-50\mu$m), are optimal for unbiased searches for AGN (Treister et al. 2005). While recent results from *Spitzer* are finding many AGN via their IR emission, IR selection is hampered by several effects (Barmby et al. 2006, Weedman et al. 2006, Franceschini et al. 2006): (1) the strong emission from star formation, (2) the lack of a unique "IR color" to distinguish AGN from other luminous objects (Stern et al. 2005), and (3) the wide range in IR spectral parameters (Weedman et al. 2006). Thus, while an IR survey yields many objects, it is very difficult to quantify its completeness and how much of the IR luminosity of a particular galaxy is due to an active nucleus. These complications are not present in a hard X-ray survey since at $E > 20$ keV virtually all the radiation comes from the nucleus and selection effects are absent for Compton thin sources. Even for moderately Compton thick sources ($\Lambda < 2.3$ is absorption $< 90\%$), a hard X-ray survey has significant sensitivity, but without an absorption correction the luminosity will be underestimated. Essentially every object more luminous that 10^{42} erg s^{-1} is an AGN. A hard X-ray survey is thus unique in its ability to find all Compton thin AGN in a uniform, well-defined fashion, and to determine their intrinsic luminosity. However, due to the relative rarity of bright AGN (even the *ROSAT* all sky survey has only $\sim$1 src deg^{-2} at its threshold — Voges et al. [1999]), one needs a very large solid angle survey to find the bright, easily studied objects.

With the recent *Chandra* and *XMM* data (e.g., Alexander et al. 2003, Giacconi et al. 2002, Yang et al. 2004; Mainieri et al. 2002, Szokoly et al. 2004, Zheng et al. 2004, Mainieri et al. 2005, Barger et al. 2001, 2003) there has been great progress in understanding the origin of the X-ray background

[1] NASA/Goddard Space Flight Center, Astrophysics Science Division, Greenbelt, MD 20771
[2] CRESST/Joint Center for Astrophysics, University of Maryland, Baltimore County, Baltimore, MD 21250
[3] CRESST/Department of Astronomy, University of Maryland College Park, College Park, MD 20742

[1]to appear in The Astrophysical Journal, July 10, 2008, v. 681

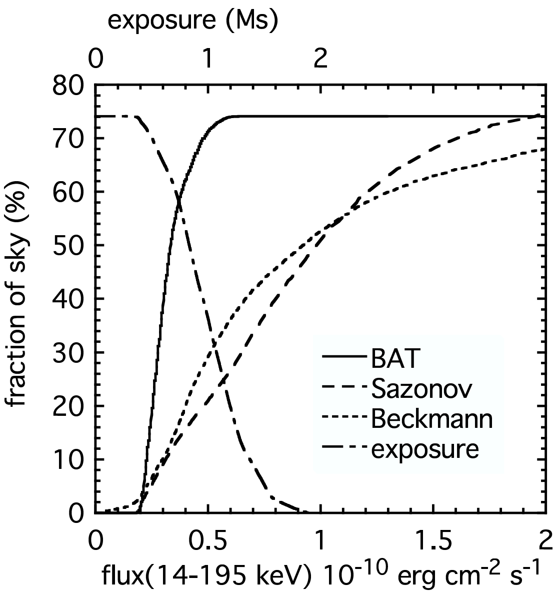

FIG. 1.— Percentage of the sky covered as a function of limiting flux in erg cm^{-2}s^{-1} (14−195 keV) and of effective exposure (upper scale). As only the sky $|b| > 15°$ is considered here, the maximum value is 74%. The corresponding curves as a function of limiting flux for the analyses of *INTEGRAL* data by Beckmann et al. (2006b) and by Sazonov et al. (2007) are shown for comparison, the flux having been converted assuming a power law spectrum with index −2.

and the evolution of AGN. It is now clear that much of the background at $E > 8$ keV is not produced by the sources detected in the $2 - 8$ keV band (Worsley et al. 2005), and is likely to come from a largely unobserved population of AGN with high column density and low redshift $z < 1$. Thus the source of the bulk of the surface brightness of the X-ray background, which peaks at E ∼30 keV (Gruber et al. 1999) is uncertain. The measurement of the space density and evolution of this putative population of highly absorbed AGN and the derivation of the distribution of their column densities as a function of luminosity and of redshift is crucial for modeling the X-ray background and the evolution of active galaxies. Progress in this area requires both a hard X-ray survey of sufficient sensitivity, angular resolution and solid angle coverage to find and identify large numbers of sources, *and* follow-up observations with softer X-ray measurements to obtain precise positions and detailed X-ray spectral properties.

Due to a lack of instrumentation with sufficient angular resolution to permit identification of unique counterparts in other wavelength bands and with sufficient solid angle and sensitivity (Krivonos et al. 2005) to produce a large sample, there has been little progress in hard X-ray surveys for over 25 years (e.g. Sazonov et al. 2005, 2007). This situation has been radically changed by the *Swift* BAT survey (Markwardt et al. 2005) and recent *INTEGRAL* results (Beckmann et al. 2006b, Sazonov et al. 2007, Krivonos et al. 2005, Bird et al. 2007) which have detected more than 100 hard X-ray selected AGN, thus providing the first unbiased sample of Compton thin AGN in the local Universe.

In this paper we describe results from the first 9 months of the hard X-ray survey using the BAT instrument (Barthelmy et al. 2005) on the *Swift* mission (Gehrels et al. 2005), concentrating on sources with $|b| > 15°$. Above this latitude limit, we have identified all but one of the sources detected at $> 4.8\sigma$ with optical counterparts using *Swift* XRT and archival X-ray data. With these same data we have also obtained X-ray spectra. With a median positional uncertainty of 1.7' and a sensitivity limit of a few times 10^{-11} erg cm^{-2} s^{-1} in the $14 - 195$ keV band, the BAT data are about 10 times more sensitive than the previous all-sky hard X-ray survey (*HEAO 1* A-4: Levine et al. 1984) and the positions are accurate enough to allow unique identifications of nearly all of the sources.

Spectra are characterized by a photon index Γ, where $N(E) \propto E^{-\Gamma}$. Luminosities are calculated using $h_{70} = 1$, $\Omega = 0.3$.

2. BAT SURVEY

The second BAT catalog is based on the first 9 months of BAT data (starting mid December 2005) and has several refinements compared to the catalog of the first 3 months of data (Markwardt et al. 2005). The combination of increased exposure, more uniform sky coverage and improved software has increased the total number of BAT sources by a factor ∼2.5.

We show the sky coverage in Figure 1 and the sensitivity of the survey as a function of exposure in Figure 2. There is a loss of sensitivity due to increased noise at low galactic latitudes from nearby bright sources, and because of spacecraft constraints there tends to be somewhat reduced exposure in directions close to the ecliptic plane. Nevertheless the sensitivity achieved is comparatively uniform.

We have picked a significance threshold of 4.8σ, which, based on the distribution of negative pixel residuals (Figure 3), corresponds to a probability of ∼1 false source in the catalog. In Table 1 we show all the sources detected at $> 4.8\sigma$ and with $|b| > 15°$. The table also includes sources that have been confidently identified with AGN but that lie at $|b| < 15°$ or, while having significances less than 4.8σ in the final analysis have appeared at higher significance in partial or preliminary analyses. Of the 44 AGN presented in Table 1 of Markwardt et al. (2005), only J1306.8−4023 does not appear in Table 1 of this study. The spectral type is from Véron-Cetty & Véron (2006), and where that is not available, we examined 6DF, SSDS or our own observations and classified the AGN. There are seven objects that do not have an optical classification, of which 2 have not been observed and the remainder do not have optical AGN lines.

We have verified the completeness of our sample by examining the values of $V/V_{\rm max}$ as a function of significance. Above 4.8σ detection significance we find a value of 0.5, as expected for a complete sample from a uniform distribution (Figure 4).

Basing the detection on significance in the total $14 - 195$ keV band is close to optimal for sources with average spectra. We might miss some sources because their spectra are much steeper. However, as shown in Figure 5, there is no apparent correlation between BAT hardness ratio and detection significance and thus we believe that this selection effect is negligible in the present sample.

Because source detection is based on the entire 9 months of data, it is possible that some sources might have been missed if they had been very bright for only a fraction of the observing time. This is confirmed by comparing the present results with those of Markwardt et al. (2005). We found that 9 of the Markwardt et al. sources do not lie above our significance threshold of 4.8σ in the 9 months data.

The accuracy of source positions (Figure 6) based on the total AGN sample, depends on significance, however, at the significance limit of 4.8σ of our survey, the maximum 2σ er-

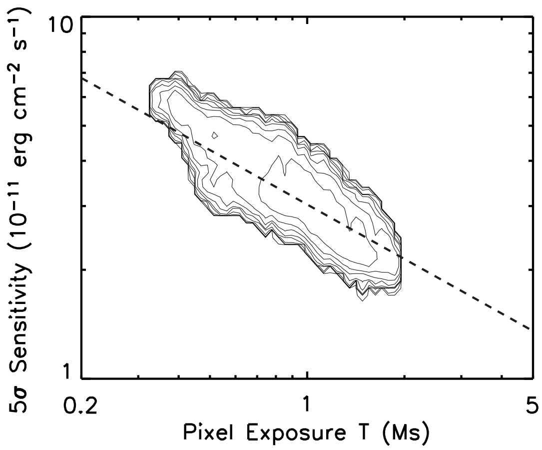

FIG. 2.— BAT survey 5σ sensitivity in the $14 - 195$ keV band for $|b| > 15^{\circ}$ as a function of exposure. The contours, spaced at logarithmic intervals, indicate the number of pixels ($|b| > 15^{\circ}$) in the all-sky mosaic with a given exposure and sensitivity. The dashed line indicates the survey sensitivity curve of Markwardt et al. (2005), without adjustment.

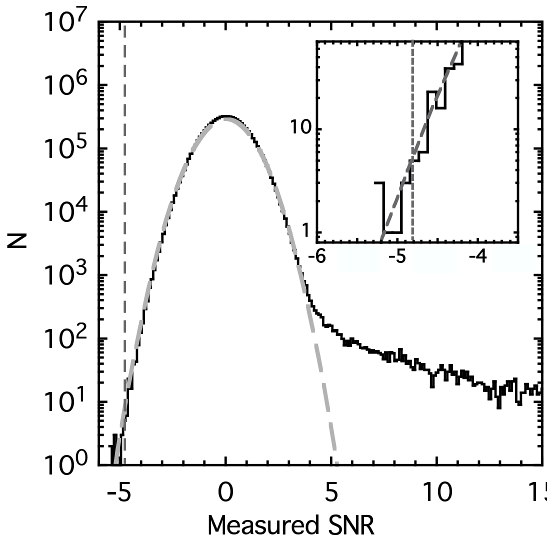

FIG. 3.— Histogram of the pixel values at $|b| > 15^{\circ}$ in the 9 month survey all sky map relative to the local estimated noise level. The data closely follow a Gaussian distribution with $\sigma = 1.024$ except for the tail at high positive values due to sources. The insert shows an expansion of the region below $SNR = -4$. Because of oversampling, more than one pixel corresponds to a single source.

ror circle radius is ∼6’.

3. SAMPLE IDENTIFICATION

BAT is a wide field ($\sim$ 2 steradians) coded aperture hard X-ray instrument (Barthelmy et al 2006). During normal operations it usually covers $\sim$ 60% of the sky each day at < 20 milliCrab sensitivity. The BAT spectra were derived from an all sky mosaic map in each energy bin averaged over 9 months of data beginning on 5 Dec 2004. The survey was processed using the BAT Ftools[4] and additional software normalize the rates to on axis and to make mosaic maps. The intrinsic binning in the BAT survey data product has 80 energy bins but to reduce processing time we used 4 energy bins for this survey. The energy bin edges are 14, 24, 50, 100, 195 keV for the 9 month survey, but will be expanded to 8 bins in the 22 month survey by dividing each of the current bins. The energies are calibrated in-flight for each detector using an on-board electronic pulser and the 59.5 keV gamma-ray line and lanthanum L and M K X-ray lines from a tagged ^{241}Am source. The average count rate in the map bin that contains the known position of the counterpart was used. Due to the the strong correlation of the signal in adjacent map bins of the oversampled coded aperture image, it is not necessary to perform a fit to the PSF. Each rate was normalized to the Crab nebula rate using an assumed spectra of $10.4E^{-2.15}$ ph cm^{-2} s^{-1} keV^{-1} for the BAT energy range. Due to the large number of different pointings that contribute to any position in the map, this is a good approximation of the average response. This has been verified by fitting sources known to have low variability and generally produces a good connection to X-ray spectra in sources. Error estimates were derived directly from the mosaic images using the RMS image noise in a region around the source of roughly 3° in radius. This is the optimum procedure due to the residual systematic errors of 1.2 to 1.8 times statistical values in the current BAT mosaics. Analysis of the noise in the images suggests that the variations in noise are small on this scale. Analysis of negative fluctuations shows that the noise is very well fit by a Gaussian distribution and that this normalization is very accurate on average. All fitting of the BAT data was performed on this normalized data using a diagonal instrument response matrix. This procedure correctly accounts for instrumental systematics in sources with spectral indices similar to the Crab. While there may be significant systematic errors for sources with spectra that are much flatter than the Crab, this is not a significant problem for any of the sources presented in this paper.

[4] `http://heasarc.nasa.gov/ftools/ftools_menu.html`

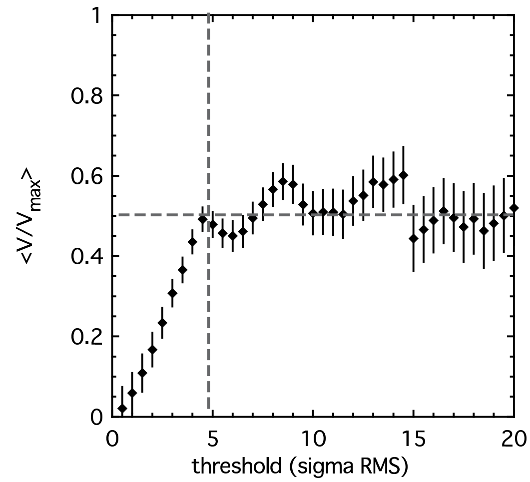

FIG. 4.— Plot of $< V/V_{\rm max} >$ as a function of the significance threshold σ. For $\sigma > 4.5$ the average ratio is consistent with the nominal $< V/V_{\rm max} >$ value of 0.5.

We first attempted to identify the BAT sources using archival X-ray, optical, and radio data. The typical high galactic latitude BAT source is a bright (2MASS J band magnitude > 13) and nearby ($z < 0.1$) galaxy. While the counterpart is often a *ROSAT* or radio source, this is not a reliable indicator. In particular we found little or no correlation between the BAT counting rates and the *ROSAT* all-sky survey fluxes (Figure 7), making it difficult or impossible to utilize the *ROSAT* data to consistently identify the sources. An examination of random

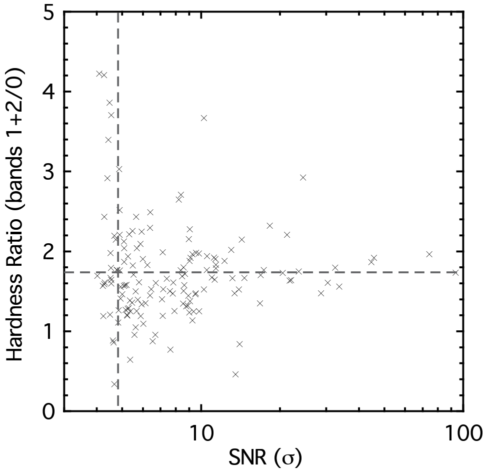

FIG. 5.— Hardness ratio (Counts [25 − 100 keV]/Counts [14 − 25 keV]) as a function of detection significance. There is no indication of discrimination against sources with soft spectra near the 4.8σ survey threshold.

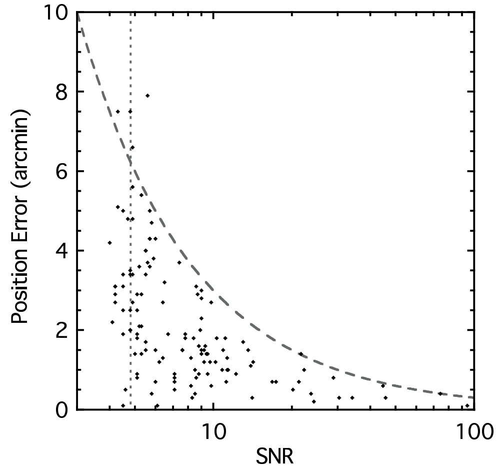

FIG. 6.— The distribution of mean offsets between positions measured with BAT and the counterpart as a function of the detection significance, *SNR*. The dashed line corresponds to $30/SNR$, or 6 arcmin at 5σ significance. The vertical dotted line is at the 4.8σ threshold used in this study. Sources below this threshold are not complete and have been identified because their known spectrum is consistent with the BAT result. Note that near the threshold the errors can occasionally be larger than this model predicts.

positions suggests this type of source rarely falls in a BAT error circle. While this approach was fruitful, we found a significant number of objects with either no obvious counterpart or multiple possible counterparts, due to clustering. We have followed up with *Swift* XRT all but one of the BAT sources in the second catalog that did not have evident identifications with previously known AGN, or that did not have archival X-ray measurements of absorption column n_H from *XMM*, *ASCA*, *Chandra* or *Beppo-Sax*. We find that if the *Swift* XRT exposure is on the order of 10 ks or greater, we have a high probability of identifying an appropriate candidate. We define an appropriate candidate as one which is within the BAT 2σ error contour and whose X-ray flux is commensurate with the BAT detection. Because of the possibility of source variability and of the low time resolution possible with the BAT data ($\sim$2 weeks per significant data point) we require only that the X-ray flux is consistent with an absorbed power law model that has a flux within a factor of ten of that predicted from the BAT detection. A detailed analysis of the variability of the BAT data is presented in Beckmann et al (2006b) and a comparison of the XRT and other data in Winter et al (2008a).

We have based our identifications on observations in the harder, $2 - 10$ keV, part of the XRT band to minimize the probability of a false identification. A *Swift* XRT detection limit of 0.001 ct s^{-1}, or 10 total counts $(0.5 - 10)$ keV in a 10 ks exposure, corresponds to a $0.5 - 10$ keV flux of about 3.7×10^{-14} erg cm^{-2} s^{-1} for an unabsorbed source or to 6.3×10^{-14} erg cm^{-2} s^{-1} for one with an average n_H of 10^{22}. Using the Moretti et al. (2003) $\log N - \log S$ distribution based on *Chandra* data there are $\sim$50 or 20 sources deg^{-2}, respectively, at these levels. Thus the probability of finding a detectable source falling by chance within a 2σ BAT error circle (6' radius at threshold) is high. However most of these sources would be expected to have a very low flux in the BAT band and thus not be candidates for the counterparts of the BAT sources. We select the brightest source or sources at energies > 3 keV as possible counterparts. A joint fit to the BAT and XRT data is performed using a simple spectral model (partially covered power law) and allowing the relative normalization between the BAT and XRT data to be a free parameter to account for variability. Agreement is defined as a relative normalization factor < 10. A more complex model is not usually required because the XRT data has insufficient statistical significance to constrain complex models. See Winter et al (2008a) for a complete description. More complex models are required in a few cases where our sources have very high column densities or are Compton thick (Winter et al. 2008c). These cases are flagged in the table as complex. We have used similar criteria for identifications based on archival data from other missions.

When an XRT counterpart has been found, the error circle radius is $\sim$4", and at the brightness of the optical counterparts (see below), there is a very high probability of identifying the object in 2MASS or DSS imaging data. For all but one of the $|b| > 15°$ sources there is a redshift in the literature (based on NED), or from our follow-up program (Winter et al. 2008c) but often there is not an available optical spectrum. Thus a significant number of the objects do not have certain optical classifications. We have used the optical spectral types reported in Véron-Cetty & Véron (2006) for AGN, where available. In other cases we have used our own optical classifications based on SDSS or 6dF on-line data or what is available in NED and SIMBAD. We show in Figure 8 some of the optical counterparts and the XRT error circles.

With these criteria we have only one unidentified source out of 130 sources with $\sigma > 4.8$ and $|b| > 15°$, but 13 out of 150 at $|b| < 15°$. This difference arises from the much higher density of stars at lower galactic latitudes and to the high degree of reddening and lack of large spectroscopic surveys in the galactic plane. The relative completeness of the identifications in the BAT survey data contrasts with that of the *INTEGRAL* data (Masetti et al. 2006a), and Bird et al. 2007 and is due to the extensive XRT follow-up and the accurate positions possible with the XRT. The one unidentified high latitude source above 4.8σ, SWIFT J1657.3+4807, has no reasonable X-ray counterpart in the XRT field of view. Obvious possibilities are (1) that this source is a transient, or (2) that it has an extraordinarily high column density such that the flux in the $2 - 10$ keV band is reduced by a factor of $\sim$300, e.g., a line of sight column density of $> 3 \times 10^{24}$ cm^{-2}, or a line of sight Compton optical depth of 2 (which would also

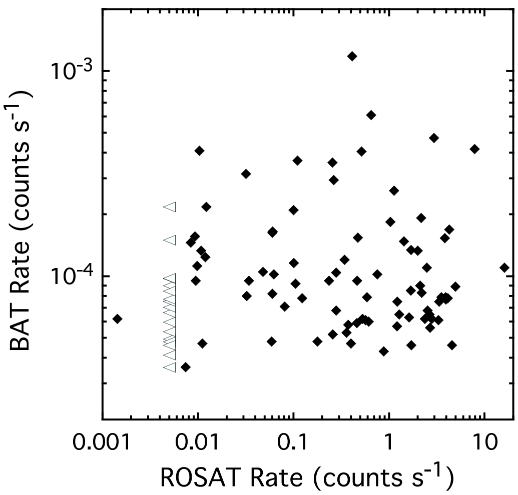

FIG. 7.— Comparison of *ROSAT* and BAT fluxes. Triangles indicate upper limits.

require that there be no scattering into the line of sight greater than 0.2%), or (3) that it is a "false" source, of which we expect ~ 1 in the survey above our significance threshold.

We have examined the BAT light curves of all of the sources in Table 1 (including those below the 4.8σ threshold) and have determined that the sources SWIFT J0201.9-4513, SWIFT J0854.2+7221, SWIFT J1319.7-3350, SWIFT J1328.4+6928 are almost certainly transients.

4. RESULTS

4.1. *Log N-Log S*

When investigating the $\log N - \log S$ law, correct allowance for sky coverage near the detection threshold is crucial. The sky coverage as a function of limiting flux that we have used (Figure 1) was obtained using the same measured RMS noise in the 9 month all-sky image that was used in assessing source significances. This direct measure of sky coverage is much more reliable than measures based on exposure as the systematic noise level varies across the sky and is not a simple function of exposure. At high fluxes the main uncertainties are due to Poisson statistics with a small number of objects. At low fluxes they are associated with the correction for completeness, which is a strong function of the flux, that is itself uncertain.

The $\log N - \log S$ distribution (Figures 9, 10) is well fit by the standard $S^{-3/2}$ function for uniformly distributed sources and a normalization of 142.63 ± 9.864 AGN with flux $> 3 \times 10^{-11}$ erg cm^{-2} s^{-1}. Formally we find a slope of 1.42 ± 0.14. Using a spectral slope for each object, we can compare this $\log N - \log S$ law with those derived from *INTEGRAL* data (Beckmann et al. 2006b, Krivinos et al. 2005, Sazonov et al. 2007). Converting our $\log N - \log S$ into the Krivinos et al. $17 - 60$ keV band we find a normalization which is $\sim$70% of their value. Conversion into the $20 - 40$ keV band leads to 50% of the Beckmann et al. value. The most likely explanation of these differences lies in the conversion factors used to convert BAT or *INTEGRAL* counts to erg s^{-1} (i.e., the instrument calibrations). The Crab spectrum used by the Krivonos et al. group for *INTEGRAL* calibration is $10 \times E^{-2.1}$ (see Churazov et al. 2007 for a detailed discussion of the use of the Crab nebula as a calibrator). The BAT team uses $10 \times E^{-2.15}$. In the $20 - 60$ keV band the *INTEGRAL* normalization gives a Crab flux which is 1.15 higher. This would account for a normalization of the $\log N - \log S$ law higher by a factor 1.23, very close to what is seen, and consistent within the uncertainties. The closeness of the BAT sample introduces some uncertainty in the distance measurement due to the random velocities of galaxies ($\sim$ 500 km s^{-1}). To evaluate the effect of this uncertainty we have performed a Monte Carlo simulation of the luminosity function, including the uncertainty in luminosity and in distance due to the velocity error. This analysis indicates that the effect on the fitted parameters is $< 1\sigma$. The break log luminosity could be 0.2 dex higher due to this error compared with an noise error of 0.4. The largest effect was on the high luminosity slope which could be 0.3 larger due to systematics (error 0.35). These systematic errors do not substantially effect the *Swift*/BAT luminosity function at its current statistical accuracy. Thus the $\log N - \log S$ law in the $14 - 195$ keV band is now established to $\sim$25% accuracy $-$ we know the number of sources quite accurately, but we do not know their flux to better than 15%.

4.2. *Luminosity Function*

The high identification completeness of our survey and the good understanding of the sky coverage are important in finding the luminosity function. We use the standard broken power law form

$$\Phi(L_X) = \frac{A}{\left[\left(\frac{L_X}{L_*}\right)^a + \left(\frac{L_X}{L_*}\right)^b\right]}, \tag{1}$$

This provides an excellent description of the data with the parameters given in Table 2. For comparison of other observations with ours we have converted luminosities quoted in other energy bands assuming a spectrum breaking from a slope of 1.7 to a slope of 2.0 at 10 keV. The BAT luminosity function shown in Figure 11 agrees well with those obtained by Beckman et al. (2006b) and by Sazonov et al. (2007) using data from *INTEGRAL* both in terms of the slopes and the break luminosities, though their errors are generally somewhat larger. However we find a significantly lower break luminosity than found by Barger et al. (2005) and by La Franca et al. (2005) from observations at lower energies. The rather large difference cannot be caused by spectral conversion factors that neglect absorption in the $2 - 10$ keV band, since this would make the observed $2 - 10$ keV luminosity even lower compared to the $14 - 195$ keV value, exacerbating the problem. We thus believe that the disagreement between the luminosity functions is due to a deficit of objects at $\log L$(erg s^{-1})< 44.11 in the $2 - 10$ keV band. Considering that the bulk of the objects and their emitted luminosity lies near the break luminosity, this could imply a substantial modification to the present day evolution models (e.g., Gilli, Comastri & Hasinger 2007).

As we show in the next section, the probability of an object being absorbed is a function of $14 - 195$ keV luminosity. Hence there is a strong selection against detecting low luminosity AGN in softer X-ray surveys (see the discussion in Sazonov et al. 2007).

4.3. *Nature of the Identifications*

There are 151 sources in Table 1 which we have identified with AGN. 102 are at high latitude ($|b| > 15°$) and above 4.8σ and form our complete sample. The remainder are at low latitude (42) and/or have lower significance in the final analysis (44). In the complete sample 14 out of 102 are beamed

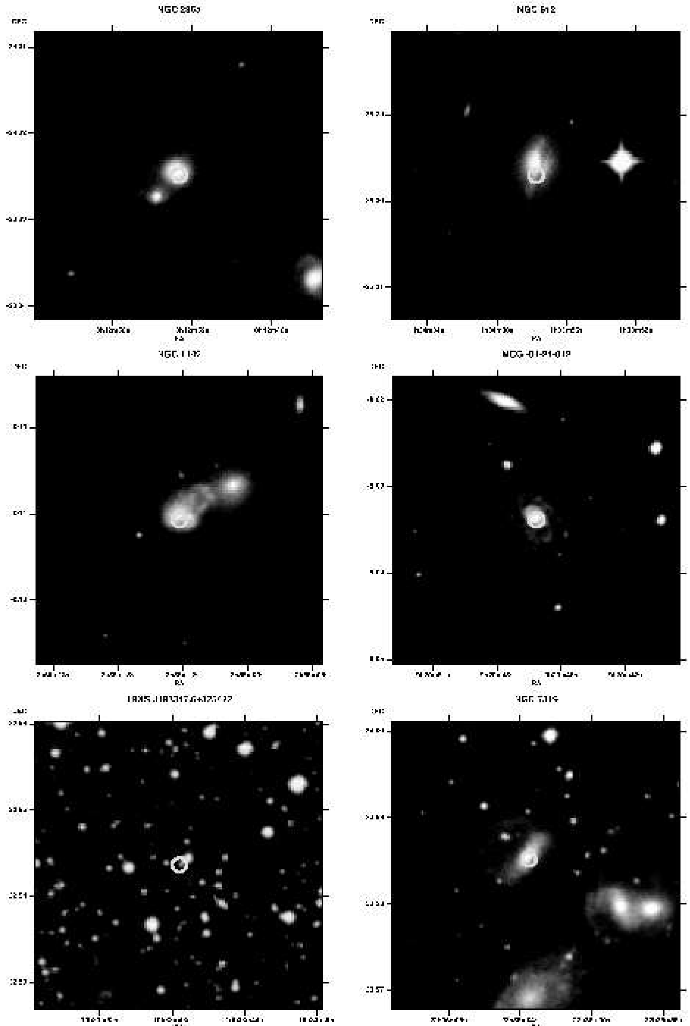

FIG. 8.— Examples of the optical counterparts and the XRT error circles for sources detected with BAT.

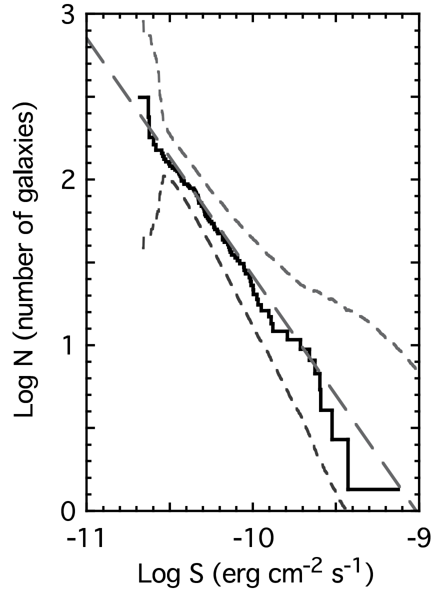

FIG. 9.— *Log N − Log S* distribution for the BAT selected AGN. S is in units of erg cm^{-2} s^{-1} in the energy range 14−195 keV. The short-dashed lines show the 99% confidence contours observed in Monte-Carlo simulations of observations of sources with a constant space density and the long-dashed lines a slope of -1.5. The long-dashed line is derived from the best fit to the differential spectrum in Figure 10.

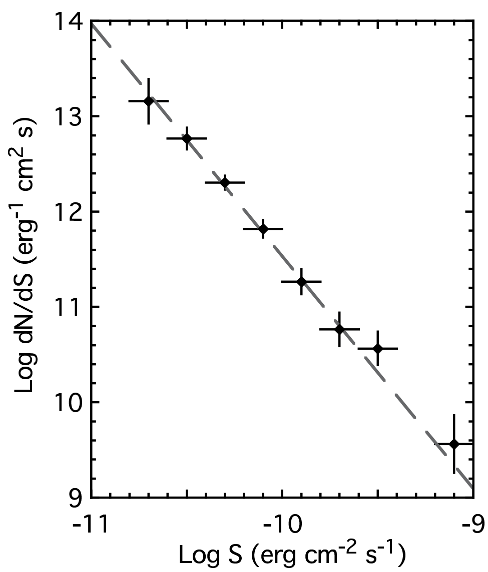

FIG. 10.— The differential $Log\,N - Log\,S$ distribution corresponding to Figure 9. The fitted line has a slope of -2.44 ± 0.14.

sources – BL Lacs and Blazars – (17 out of 152 overall) and the remainder are Seyferts and galaxies which show indications of activity. In addition, we have detected 32 galactic sources and 2 galaxy clusters which meet the latitude and significance criteria for the complete sample. At low latitudes we also detect at $> 4.8\sigma$ 103 galactic sources, 3 galaxy clusters, and 13 unidentified sources. Although they are included in Table 1, we have not used sources identified as blazar or BL Lac, nor any source with $z > 0.5$, in the distribution functions.

We use the J band magnitudes from the 2MASS survey to categorize the objects since that is the largest homogeneous data base which covers the largest fraction of the *Swift* BAT sources. It is noticeable that the faintest optical counterparts are the blazars and the galactic sources. The optically determined AGN tend to be in fairly bright galaxies. One of the reasons that there are so few blazar identifications at low galactic latitudes is the relative faintness of the likely optical counterparts combined with the lack of available redshifts and the effect of galactic reddening.

Nine of the objects have not previously been optically classified as AGN. An excellent example of this is the object NGC 4138 (Ho 1999, Moustakas & Kennicutt 2006) which shows little or no [OIII] emission and in which only very high signal to noise spectra revealed a very faint broad Hα line. Other objects, like NGC4102 (Moustakas & Kennicutt 2006) show no optical evidence of AGN activity.

For those objects which are optically classified as AGNs, 33 are Seyfert 1s, 14 are Seyfert 1.5, 35 are Seyfert 2s. There is reasonable but not perfect correlation between the optical classification and the presence of X-ray absorption (see below). Only two of 33 Seyfert 1's have a column density greater than 10^{22} cm^{-2}, whereas 4 of 14 Seyfert 1.5's and 33 of 35 Seyfert 2's are absorbed (two do not have X-ray column densities).

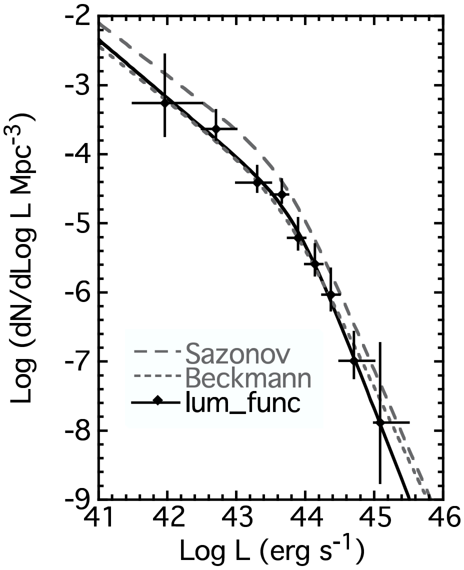

FIG. 11.— Comparison of the 14−195 keV luminosity function derived from the BAT observations with those found by Beckmann (2006b) and by Sazonov et al. (2007) using *INTEGRAL*. The *INTEGRAL* luminosities have been converted to the BAT band assuming an power law with photon index of 2.0.

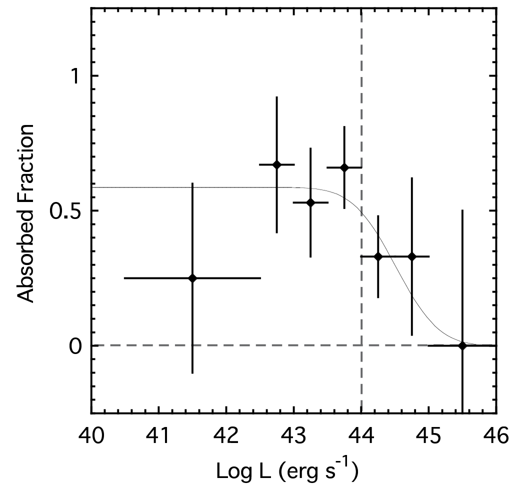

FIG. 13.— The fraction of BAT selected AGN with $n_H > 10^{22}$ cm^2 as a function of 14−195 keV luminosity. The position of the break in the luminosity function slope is indicated. The smooth curve is simply one form which is consistent with the data. As elsewhere, only AGN with $|b| > 15°$ and significance greater than 4.8σ have been included. We note that if AGN with $|b| < 15°$ are included the drop at high luminosity is less pronounced but it is still significant at the $> 2\sigma$ level.

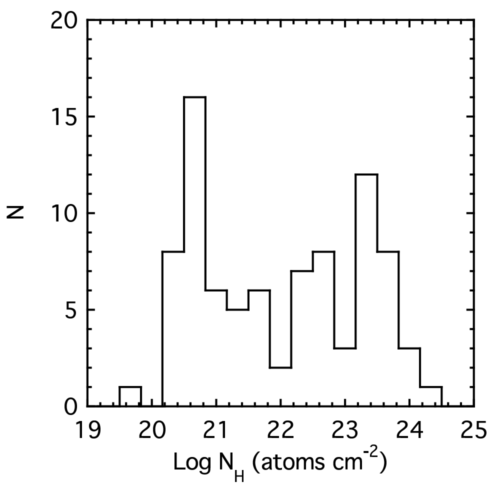

FIG. 12.— The distribution of column densities for the BAT selected AGN. Notice the peak at low column densities and the relatively flat distribution above it. The galactic column density has not been subtracted.

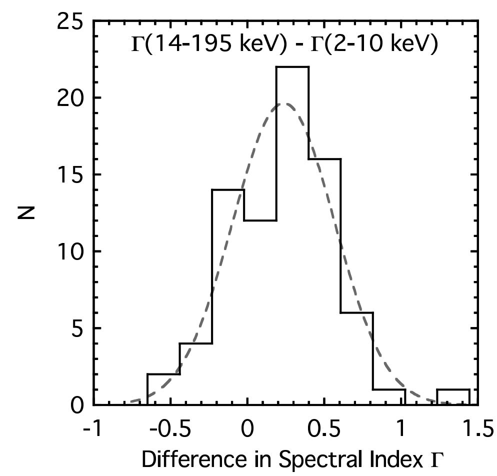

FIG. 14.— Histogram of the X-ray spectral index in the BAT band minus the X-ray spectral index. The X-ray indices are mostly from *ASCA* and XRT with some from various other missions. The mean difference is 0.26 with a standard deviation of 0.36.

The median redshift of the non-blazars is ~ 0.017. However, the blazar redshift distribution is very different with a long tail to high redshift and a median redshift of 0.24 (mean of 0.76). Thus we have been careful in determining the overall luminosity function to separate the blazars from the non-blazars since this will significantly change the slope of the high luminosity end of the luminosity function.

4.4. *X-ray Spectral Analysis*

The X-ray spectra of many of the sources have been published (see the references in Table 1). In these cases we have used the previously reported values of the column densities of the sources, while noting that the signal to noise of the observations varies greatly, as does the sophistication of the analysis and the type of models used to classify the spectra. Many of the spectra are rather complex (Winter et al. 2008a), making assignment of errors to the column density difficult and highly model dependent. Where the column densities in Table 1 were obtained with *Swift* XRT follow-up observations, for homogeneity we report the results of simple absorbed power law fits. As shown in Figure 7, a large fraction of the BAT sources are not detected by the *ROSAT* all sky survey, despite its factor of 100 better sensitivity for unabsorbed sources. This graphically illustrates the importance of obscuration in the selection of X-ray samples.

A detailed analysis of the archival *XMM*, *ASCA*, *BeppoSax*, and *Chandra* data as well as the *Swift* XRT data will presented in another paper (Winter et al. 2008a).

The distribution of absorption for the non-blazars (Figure 12) is almost flat for $\log n_H(\mathrm{cm}^{-2})$ in the range $21-24$, with a strong peak at low column density due primarily to the effects of galactic obscuration. The relative paucity of Compton thick objects ($\log n_H[\mathrm{cm}^{-2}] \geq 24.5$) is interesting. Unfortunately at such high columns the flux, even in the BAT energy band,

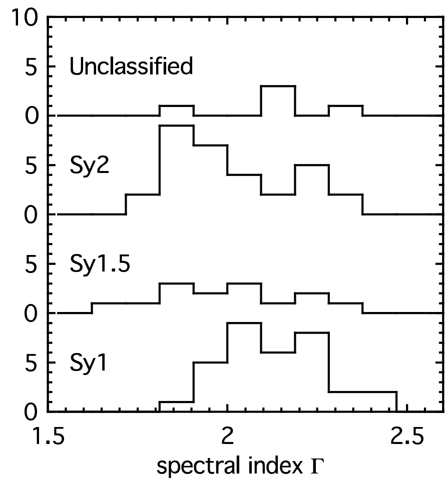

FIG. 15.— Distribution of power law indices in the $14-195$ keV band for BAT selected sources sorted into Seyfert 1, Seyfert 1.5, Seyfert 2 and unclassified objects.

is severely reduced so our level of completeness is uncertain. In addition we are only able to fit simplified models for many of these objects. Thus quantification of the lack of Compton thick objects awaits more observations with high sensitivity X-ray spectrometers (e.g., *XMM*, *Suzaku*).

As shown in Figure 13, the fraction of strongly absorbed AGN drops with increasing luminosity. This is consistent with the previous claims of a drop in the absorbed fraction at higher luminosities, but it is not yet of sufficient statistical significance to confirm this dependence. While this has been seen in several X-ray selected surveys (Ueda et al. 2003, La Franca et al. (2005), Shinozaki et al. 2006), the fact that the selection of BAT sources is independent of the line of sight column density confirms and extends these results.

4.5. *BAT Spectral Analysis*

At the present stage of analysis we only have four channel spectra available (this is a limitation of the present analysis software and is not intrinsic to the experiment). We have thus fit only simple power law models to the data.

The fact that the BAT hardness ratio shows no correlation with signal-to-noise (Figure 5) indicates that there is no selection bias due to spectral parameters. The median spectral index is $\Gamma = 1.98$, in agreement with the *INTEGRAL* results from Beckmann et al. (2006b), with an *rms* spread 0.27. For a sample of 74 sources which have archival X-ray spectrum spectra at lower energies (e.g., Markowitz & Edelson 2004), the BAT slope is on average ~ 0.23 steeper than in the X-ray band (Figure 14). A viable explanation for this (Nandra et al. 1999) is that the BAT data are detecting the "true" X-ray spectral slope of 2, while the X-ray data are strongly influenced by the effects of reflection. Malizia et al. (2003) found using *BeppoSAX* hard X-ray data that Seyfert 2s are systematically harder than Seyfert 1s. A similar result is reported by Beckmann et al. (2006a). Comparison of the spectral index distributions of Seyfert 1 and Seyfert 2s (Figure 15) confirms this finding – according to a Kolmogorov-Smirnov test the two distributions have a probability of less than 0.1% of arising from the same parent distribution function.

5. DISCUSSION

5.1. *Luminosity Function*

As shown above the low luminosity slope of the luminosity function of hard X-ray selected AGN is steeper than that of the $2-8$ keV function of Barger et al. 2005. We believe that this is due to the high fraction of heavily absorbed objects at low BAT luminosities. Thus the contribution of low luminosity objects to the $10-100$ keV background is larger than originally calculated. This is confirmed by the agreement of the slope of our luminosity function with the absorption corrected low luminosity slope of La Franca et al. (2005), which unlike Barger et al (2005) assumes an absorption that depends on luminosity. The break in the luminosity function is quite robust and thus is an intrinsic feature of the luminosity function and is not due to a spectral selection effect. Integration of our luminosity function gives a local volume density of $n(L_X > 10^{41}\mathrm{erg\ s}^{-1}) = 2.4\times10^{-3}$ Mpc^{-3}, compared to a density of 0.02 Mpc^{-3} galaxies brighter than $M_* = -19.75$ (Cross et al. 2001), and a local emissivity of 2.3×10^{39} erg s^{-1} Mpc^{-3}. The choice of M_* is that is the knee in the luminosity function and is the typical absolute magnitude for a galaxy. It is a simple way of estimating the galaxy density. The typical J band absolute magnitude at the knee is $M* = -21.73$ (Cole et al 2001). The median BAT J band absolute magnitude is $M = -23.8$ and only 3 BAT AGN have $M > -22$. Hence $\gtrsim 10\%$ of luminous galaxies in the local Universe are AGN with a hard X-ray luminosity $\gtrsim 10^{41}$ erg s^{-1}. Because of the low median redshift of the sample, the BAT data are not sensitive to evolution in the luminosity function and $V/V_{\max}$ ~0.5 is as expected.

5.2. *Log N-Log S*

There have been numerous predictions of the hard X-ray $\log N - \log S$ (Treister et al. 2006, Gandhi & Fabian 2003) and our data allow a direct comparison of these models. We find that converting the observed BAT $\log N - \log S$ to the band predicted by these authors that we have good agreement with the predictions of Gandhi et al. (2004), but lie a factor of 2 lower than that predicted by Treister et al. (2006). Since each of these models makes different assumptions, our hard X-ray survey should be able to determine which are valid.

5.3. *The distribution of n_H*

In Figures 13 and 15 the distribution of column densities over all objects is almost flat and appears to depend on hard X-ray luminosity. Similar results based on the *RXTE* slew survey were obtained by Sazonov & Revnivtsev (2004). The standard unified model predicts that the ratio of absorbed to unabsorbed objects should be $4:1$, as opposed to our observed value of $1:1$. This difference is probably due to the neglect of the luminosity dependence of absorption in the simple unified model. The BAT results are roughly consistent with dependence of absorption on luminosity seen previously (Ueda et al. 2003, Steffen et al. 2003, Gilli et al. 2007). We note that the distribution of column densities in Tozzi et al. (2006) from the *Chandra* deep fields is rather different from the BAT sample in that the Tozzi et al. sample seems to be missing the low n_H half of the distribution. This has been confirmed by Wang et al. (2007) and by Gilli et al. (2007). Direct comparison of the n_H distribution from the BAT sample and Tozzi et al shows apparent differences, especially at low n_H. Taken at face value, this would indicate an evolution of the n_H distribution between the low median redshift of the BAT sample (0.03) and the redshift of the Tozzi sample (~ 0.7). This is similar to the results reported by La Franca et

al. (2005), however Hasinger et al (2008) find no such dependence.

6. CONCLUSION

We have presented the results of an AGN survey using data from the BAT instrument on *Swift*. The use of a hard X-ray bandpass means that the survey is immune to the effects of X-ray absorption that have traditionally plagued similar studies in optical and soft X-ray bandpasses, raising serious questions concerning completeness. Utilizing the standard AGN broken power law prescription to characterize the differential luminosity distribution function, we find that the data can be very well described taking a break luminosity $\log L_*(\text{erg s}^{-1}) = 43.85 \pm 0.26$, a low luminosity power law slope $a = 0.84^{+0.16}_{-0.22}$, and a high luminosity power law slope $b = 2.55^{+0.43}_{-0.30}$, in agreement with other studies based on hard X-ray survey data such as that of Sazonov et al. (2007) using *INTEGRAL*. We find a median spectral index 1.98, in accord with the Beckmann et al. (2006b) study using *INTEGRAL*. By integrating our inferred luminosity function above 10^{41} erg s^{-1}, we arrive at a local volume density of 2.4×10^{-3} Mpc^{-3}, roughly 10% of the local density of luminous galaxies.

The BAT survey has detected 31 AGN at $> 4.8\sigma$ that were not previously detected in hard X-rays, of which 9 were not previously identified as AGN by other techniques. In addition, there are 14 BAT AGN that were also detected contemporaneously in hard X-rays by *INTEGRAL*, of which 5 had not been previously identified as AGN. For sources that were detected by both instruments, there is a good correlation between the BAT and *INTEGRAL* flux, with the exception of a few sources that are almost certainly variable. There are 42 *INTEGRAL* AGN with SNR > 4.8 that were not detected by BAT. Only 11 of these have a flux (scaled to the BAT energy band assuming E^{-2} spectrum) that is greater than 3×10^{-11} erg cm^{-2} s^{-1}, where a BAT detection is likely. Most of these high-flux, undetected sources are within 30° of the Galactic Center, where the BAT survey has significantly reduced sensitivity due to lower exposure and increased systematic errors. Of the BAT detected sources, 13% were not previously known to be AGN.

With increased exposure, both the BAT and *INTEGRAL* survey sensitivities will improve, and we expect most of the new unidentified hard X-ray sources to be in the interesting class of very heavily absorbed AGN. *INTEGRAL* detected 111 AGN at $> 4.8\sigma$ in ~ 4 yr. Due to its larger FOV and random observing strategy, BAT detected 126 AGN in 0.75 yr, a rate 6 times faster than *INTEGRAL*. We expect both missions to continue accumulating new AGN at the same rates, in which case BAT AGN will become an increasing fraction of the new detections. At 3 yr after the *Swift* launch, we predict 450 BAT detected AGN and more than 60 that not have been previously identified as AGN. The hard X-ray measurements are unique in another sense. We believe they yield a accurate measurement of the average luminosity of these sources. We have shown (Winter et al. 2008bc) that the luminosity and power law index for absorbed sources cannot be accurately derived from $2-10$ keV X-ray measurements alone, even with *XMM* or *Chandra*. For the $\sim 1/2$ of all AGN that are absorbed, the BAT and *INTEGRAL* surveys provide a unique new measurements of the luminosity and underlying power law.

This is the second paper in a series. In future papers we will present the X-ray spectral properties of these objects, the long term BAT light curves, detailed spectral analysis of the BAT data and the optical properties of the hosts of the BAT sources, and extend the sample by a factor of two in size.

REFERENCES

Akylas, A., Georgantopoulos, I., Griffiths, R. G., Papadakis, I. E., Mastichiadis, A., Warwick, R. S., Nandra, K., & Smith, D. A. 2002, MNRAS, 332, L23
Alexander, D. M., et al. 2003, AJ, 126, 539
Alonso-Herrero, A., et al. 2006, ApJ, 640, 167
Ballantyne, D. R. 2005, MNRAS, 362, 1183
Barger, A. J., Cowie, L. L., Mushotzky, R. F., & Richards, E. A. 2001, AJ, 121, 662
Barger, A. J., Cowie, L. L., Capak, P., Alexander, D. M., Bauer, F. E., Fernandez, E., Brandt, W. N., Garmire, G. P., & Hornschemeier, A. E. 2003, AJ, 126, 632
Barger, A. J., Cowie, L. L., Mushotzky, R. F., Yang, Y., Wang, W.-H., Steffen, A. T., & Capak, P. 2005, AJ, 129, 578
Barmby, P., et al. 2006, ApJ, 642, 126
Barthelmy, S. D., et al. 2005, Space Science Reviews, 120, 143
Bassani, L., Dadina, M., Maiolino, R., Salvati, M., Risaliti, G., della Ceca, R., Matt, G., & Zamorani, G. 1999, ApJS, 121, 473
Beckmann, V., Gehrels, N., Shrader, C. R., & Soldi, S. 2006a, ApJ, 638, 642
Beckmann, V., Soldi, S., Shrader, C. R., Gehrels, N., & Produit, N. 2006b, ApJ, 652, 126
Bikmaev, I. F., Sunyaev, R. A., Revnivtsev, M. G., & Burenin, R. A. 2006, Astronomy Letters, 32, 221
Bird, A. J., et al. 2007, ApJS, 170, 175
Brandt, W. N. & Hasinger, G. 2005, ARA&A, 43, 827
Brinkmann, W., Otani, C., Wagner, S. J., & Siebert, J. 1998, A&A, 330, 67
Burenin, R., Mescheryakov, A., Revnivtsev, M., Bikmaev, I., & Sunyaev, R. 2006, The Astronomer's Telegram, 880, 1
Cappi, M., et al. 2006, A&A, 446, 459
Churazov, E., et al. 2007, A&A, 467, 529
Cole, S., et al. 2001, MNRAS, 326, 255
Cross, N., et al. 2001, MNRAS, 324, 825
Donzelli, C. J. & Pastoriza, M. G. 2000, AJ, 120, 189
Evans, D. A., Worrall, D. M., Hardcastle, M. J., Kraft, R. P., & Birkinshaw, M. 2006, ApJ, 642, 96
Franceschini, A., et al., 2006, A&A, 453, 397
Gallo, L. C., Lehmann, I., Pietsch, W., Boller, T., Brinkmann, W., Friedrich, P., & Grupe, D. 2006, MNRAS, 365, 688
Gandhi, P., Crawford, C. S., Fabian, A. C., & Johnstone, R. M. 2004, MNRAS, 348, 529
Gandhi, P. & Fabian, A. C. 2003, MNRAS, 339, 1095
Gehrels, N., et al. 2004, ApJ, 611, 1005
Giacconi, R., et al. 2002, ApJS, 139, 369
Gilli, R., Comastri, A., & Hasinger, G. 2007, A&A, 463, 79
Gilli, R., Maiolino, R., Marconi, A., Risaliti, G., Dadina, M., Weaver, K. A., & Colbert, E. J. M. 2000, A&A, 355, 485
Giommi, P., Piranomonte, S., Perri, M., & Padovani, P. 2005, A&A, 434, 385
Gondoin, P., Orr, A., Lumb, D., & Siddiqui, H. 2003, A&A, 397, 883
Gruber, D. E., Matteson, J. L., Peterson, L. E., & Jung, G. V. 1999, ApJ, 520, 124
Halpern, J. P. 2006, The Astronomer's Telegram, 847, 1
Heckman, T. M., Ptak, A., Hornschemeier, A., & Kauffmann, G. 2005, ApJ, 634, 161
Ho, L. C. 1999, ApJ, 516, 672
Immler, S., Brandt, W. N., Vignali, C., Bauer, F. E., Crenshaw, D. M., Feldmeier, J. J., & Kraemer, S. B. 2003, AJ, 126, 153
Kennea, J. A., et al. 2005, The Astronomer's Telegram, 677, 1
Kraft, R. P., Hardcastle, M. J., Worrall, D. M., & Murray, S. S. 2005, ApJ, 622, 149
Krivonos, R., Vikhlinin, A., Churazov, E., Lutovinov, A., Molkov, S., & Sunyaev, R. 2005, ApJ, 625, 89
La Franca, F., et al. 2005, ApJ, 635, 864
Lawson, A. J. & Turner, M. J. L. 1997, MNRAS, 288, 920
Levine, A. M., et al. 1984, ApJS, 54, 581
Lewis, K. T., Eracleous, M., & Sambruna, R. M. 2003, ApJ, 593, 115
Lutz, D., Maiolino, R., Spoon, H. W. W., & Moorwood, A. F. M. 2004, A&A, 418, 465
Mainieri, V., Bergeron, J., Hasinger, G., Lehmann, L., Rosati, P., Schmidt, M., Szokoly, G., Della Ceca, R. 2002, A&A, 393, 425

Mainieri, V., et al. 2005, A&A, 437, 805
Maiolino, R., Salvati, M., Bassani, L., Dadina, M., della Ceca, R., Matt, G., Risaliti, G., & Zamorani, G. 1998, A&A, 338, 781
Malizia, A., Bassani, L., Stephen, J. B., Di Cocco, G., Fiore, F., & Dean, A. J. 2003, ApJL, 589, L17
Markowitz, A. & Edelson, R. 2004, ApJ, 617, 939
Markwardt, C. B., Tueller, J., Skinner, G. K., Gehrels, N., Barthelmy, S. D., & Mushotzky, R. F. 2005, ApJL, 633, L77
Masetti, N., Mason, E., Bassani, L., Bird, A. J., Maiorano, E., Malizia, A., Palazzi, E., Stephen, J. B., Bazzano, A., Dean, A. J., Ubertini, P., & Walter, R. 2006a, A&A, 448, 547
Masetti, N., et al. 2006b, A&A, 459, 21
Matt, G., Fabian, A. C., Guainazzi, M., Iwasawa, K., Bassani, L., & Malaguti, G. 2000, MNRAS, 318, 173
Meléndez, J., et al. 2008, in preparation
Molina, M., et al. 2006, MNRAS, 371, 821
Morelli, L., Masetti, N., Bassani, L., Landi, R., Malizia, A., Bird, A. J., Ubertini, P., & Galaz, G. 2006, The Astronomer's Telegram, 785, 1
Moretti, A., Campana, S., Lazzati, D., & Tagliaferri, G. 2003, ApJ, 588, 696
Moustakas, J. & Kennicutt, Jr., R. C. 2006, ApJS, 164, 81
Mushotzky, R. F., et al. 2007, in preparation
Nandra, K., George, I. M., Mushotzky, R. F., Turner, T. J., & Yaqoob, T. 1999, ApJL, 523, L17
Perlman, E. S., et al. 2005, ApJ, 625, 727
Predehl, P. & Schmitt, J. H. M. M. 1995, A&A, 293, 889
Reynolds, C. S. 1997, MNRAS, 286, 513
Risaliti, G., Maiolino, R., & Salvati, M. 1999, ApJ, 522, 157
Sambruna, R. M., George, I. M., Mushotzky, R. F., Nandra, K., & Turner, T. J. 1998, ApJ, 495, 749
Sambruna, R. M., et al. 2006, ApJ, 646, 23
Sargent, W. L. W. 1970, ApJ, 159, 765
Sazonov, S., Churazov, E., Revnivtsev, M., Vikhlinin, A., & Sunyaev, R. 2005, A&A, 444, L37
Sazonov, S., Revnivtsev, M., Krivonos, R., Churazov, E., & Sunyaev, R. 2007, A&A, 462, 57
Schoenmakers, A. P., Mack, K.-H., Lara, L., Roettgering, H. J. A., de Bruyn, A. G., van der Laan, H., & Giovannini, G. 1998, A&A, 336, 455
Schwope, A., Hasinger, G., Lehmann, I., Schwarz, R., Brunner, H., Neizvestny, S., Ugryumov, A., Balega, Y., Trümper, J., & Voges, W. 2000, Astronomische Nachrichten, 321, 1
Shinozaki, K., Miyaji, T., Ishisaki, Y., Ueda, Y., & Ogasaka, Y. 2006, AJ, 131, 2843
Steffen, A. T., Barger, A. J., Cowie, L. L., Mushotzky, R. F., & Yang, Y. 2003, ApJL, 596, L23
Stern, D., et al. 2005, ApJ, 631, 163
Szokoly, G. P., et al. 2004, ApJS, 155, 271
Tozzi, P., et al. 2006, A&A, 451, 457
Treister, E., et al. 2005, ApJ, 621, 104
Treister, E., et al. 2006, ApJ, 640, 603
Ueda, Y., Akiyama, M., Ohta, K., & Miyaji, T. 2003, ApJ, 598, 886
Véron-Cetty, M.-P. & Véron, P. 2006, A&A, 455, 773
Vignali, C. & Comastri, A. 2002, A&A, 381, 834
Voges, W. et al. 1999, A&A, 349, 389
Wang, J. X., et al. 2007, ApJ, 657, 95
Watanabe, C., Ohta, K., Akiyama, M., & Ueda, Y. 2004, ApJ, 610, 128
Weedman, D., 2006, ApJ, 653, 101
Winter, L. M., et al. 2008a, ApJ, 674, 686
Winter, L. M., et al. 2008b, in preparation
Winter, L. M., et al. 2008c, in preparation
Worsley, M. A., et al. 2005, MNRAS, 357, 1281
Yang, Y., Mushotzky, R. F., Steffen, A. T., Barger, A. J., & Cowie, L. L. 2004, AJ, 128, 1501
Zheng, W., et al. 2004, ApJS, 155, 73

TABLE 1
Swift SURVEY TABLE.

#	*Swift*[a] name	ID[b]	RA[c] deg	Dec[c] deg	$> 15^\circ$ [d]	SNR	$f_{\rm BAT}$ [e]	z	log L [e] erg s^{-1}	log n_H cm^{-2}	Ref. [f]	Cmplx [g]	Type [h]	Note [i]	J mag	$f_{\rm ROSAT}$ rate[j,k]
1	SWIFT J0042.9−2332	NGC 235A	10.7200	−23.5410	y	4.47	3.2	0.022229	43.56	23.00	1	y	Sy 2†		10.58	0.024
2	SWIFT J0048.8+3155[l]	Mrk 348	12.1964	31.9570	y*	13.00	9.5	0.015034	43.68	23.32	2	y	Sy 2		11.24	0.009
3	SWIFT J0059.4+3150	Mrk 352	14.9720	31.8269	y*	4.90	3.7	0.014864	43.27	20.75	3		Sy 1		12.49	0.615
4	SWIFT J0114.4−5522	NGC 454	18.5946	−55.3986	y	4.54	2.3	0.012125	42.88	22.95	1	y	Sy 2	37	13.98	
5	SWIFT J0123.9−5846[l]	Fairall 9	20.9408	−58.8057	y*	8.90	4.7	0.04702	44.39	20.36	4		Sy 1		11.85	3.350
6	SWIFT J0123.8−3504[l]	NGC 526A	20.9766	−35.0654	y*	8.20	5.2	0.019097	43.63	22.30	4	y	Sy 1.5		11.60	0.123
7	SWIFT J0134.1−3625	NGC 612	23.4906	−36.4933	y*	4.89	3.2	0.029771	43.81	23.70	5	y	Gal/Radio	38	11.68	
8	SWIFT J0138.6−4001[l]	ESO 297−018	24.6548	−40.0114	y*	9.03	4.9	0.025201	43.85	23.84	1	y	Sy 2		9.18	
9	SWIFT J0201.0−0648	NGC 788	30.2769	−6.8155	y*	8.37	5.9	0.013603	43.39	23.48	6	y	Sy 2		10.02	
10	SWIFT J0206.2−0019	Mrk 1018	31.5666	−0.2914	y*	5.31	3.5	0.04244	44.17	20.53	1		Sy 1.5		11.60	0.360
11	SWIFT J0209.7+5226	LEDA 138501	32.3929	52.4425		5.13	3.9	0.0492	44.34	21.18	1		Sy 1			0.752
12	SWIFT J0214.6−0049	Mrk 590	33.6398	−0.7667	y*	5.67	3.7	0.02638	43.77	20.43	7		Sy 1.2		10.71	2.689
13	SWIFT J0216.3+5128	2MASX J02162987+5126246	34.1243	51.4402		4.93	3.6			22.25	1		Galaxy†	40	14.27	
14	SWIFT J0218.0+7348	[HB89] 0212+735	34.3784	73.8257		4.27	2.6	2.367	48.05	23.38	1		BL Lac			0.044
15	SWIFT J0228.1+3118	NGC 931	37.0603	31.3117	y*	8.56	7.3	0.016652	43.66	21.65	8		Sy 1.5		10.40	0.342
16	SWIFT J0234.6−0848	NGC 985	38.6574	−8.7876	y*	5.07	3.7	0.043	44.21	21.59	8	y	Sy 1†		11.63	1.281
17	SWIFT J0235.3−2934	ESO 416−G002	38.8058	−29.6047	y	4.76	3.2	0.059198	44.42	< 19.60	9		Sy 1.9		12.15	0.356
18	SWIFT J0238.2−5213[l]	ESO 198−024	39.5821	−52.1923	y*	7.82	3.9	0.0455	44.27	21.00	8		Sy 1		12.68	2.380
19	SWIFT J0244.8+6227	QSO B0241+622	41.2404	62.4685		11.19	7.3	0.044	44.52	21.98	10		Sy 1			0.414
20	SWIFT J0255.2−0011[l]	NGC 1142	43.8008	−0.1836	y*	9.80	7.8	0.028847	44.17	23.38	9	y	Sy 2†		10.06	0.011
21	SWIFT J0318.7+6828	2MASX J03181899+6829322	49.5791	68.4921		4.89	3.5	0.0901	44.85	22.59	1		Sy 1.9	41	15.13	
22	SWIFT J0319.7+4132	NGC 1275	49.9507	41.5117		13.51	11.5	0.017559	43.90	21.18	11		Sy 2		11.02	4.756
23	SWIFT J0328.4−2846	PKS 0326−288	52.1521	−28.6968	y	4.50	2.3	0.108	44.84				Sy 1.9	42	14.19	
24	SWIFT J0333.6−3607[l]	NGC 1365	53.4015	−36.1404	y*	13.93	7.2	0.005457	42.67	23.60	4	y	Sy 1.8		7.36	0.101
25	SWIFT J0342.0−2115	ESO 548−G081	55.5155	−21.2444	y*	5.45	3.3	0.01448	43.19	20.48	1		Sy 1		9.35	0.258
26	SWIFT J0349.2−1159	1ES 0347−121	57.3467	−11.9908	y*	5.29	3.6	0.18	45.51	20.55	8		BL Lac			1.210
27	SWIFT J0350.1−5019	PGC 13946	57.5990	−50.3099	y*	5.99	2.9	0.036492	43.95	22.72	1		Galaxy	40	11.68	
28	SWIFT J0356.9−4041	2MASX J03565655−4041453	59.2356	−40.6960	y*	5.22	2.4	0.0747	44.51	22.52	1		Sy 1.9	42	13.27	0.007
29	SWIFT J0407.4+0339	3C 105	61.8186	3.7071	y	4.01	3.4	0.089	44.83	23.43	1		Sy 2		15.16	
30	SWIFT J0418.3+3800	3C 111.0	64.5887	38.0266		13.41	12.5	0.0485	44.84	21.98	8		Sy 1		13.63	0.398
31	SWIFT J0426.2−5711	1H 0419−577	66.5035	−57.2001	y*	5.49	2.9	0.104	44.91	19.52	8		Sy 1			4.563
32	SWIFT J0433.0+0521[l]	3C 120	68.2962	5.3543	y*	13.15	11.2	0.03301	44.45	21.19	8		Sy 1		11.69	2.174
33	SWIFT J0444.1+2813	2MASX J04440903+2813003	71.0376	28.2168		7.15	7.6	0.01127	43.33	22.72	1		Sy 2		10.88	
34	SWIFT J0451.4−0346[l]	MCG −01−13−025	72.9230	−3.8094	y*	5.62	4.5	0.015894	43.41	20.62	7		Sy 1.2		11.14	0.281
35	SWIFT J0452.2+4933	1RXS J045205.0+493248	73.0208	49.5459		7.59	5.6	0.029	44.04	21.65	1		Sy 1		12.26	0.590
36	SWIFT J0505.8−2351	XSS J05054−2348	76.4405	−23.8539	y*	11.26	6.1	0.035043	44.24	22.69	1		Sy 2		13.77	0.009
37	SWIFT J0510.7+1629	4U 0517+17	77.6896	16.4988		7.12	7.8	0.017879	43.75				Sy 1.5			0.670
38	SWIFT J0516.2−0009[l]	Ark 120	79.0476	−0.1498	y*	7.12	5.3	0.032296	44.11	20.30	4		Sy 1		11.26	2.120
39	SWIFT J0501.9−3239	ESO 362−G018	79.8992	−32.6578	y*	10.49	5.1	0.012642	43.26	20.25		y	Sy 1.5		11.10	0.060
40	SWIFT J0519.5−4545	PICTOR A	79.9570	−45.7790	y	4.23	2.2	0.035058	43.80	21.00	8		Sy 1/Liner		13.63	0.626
41	SWIFT J0519.5−3140	PKS 0521−365	80.7416	−36.4586	y*	6.02	2.8	0.05534	44.31	21.11	8		BL Lac		12.50	0.883
42	SWIFT J0538.8−4405	PKS 0537−441	84.7098	−44.0858	y*	5.79	3.1	0.8904	47.09	20.54	14		BL Lac		13.45	0.178
43	SWIFT J0539.9−2839	[HB89] 0537−286	84.9762	−28.6655	y	4.27	2.5	3.104	48.32	20.77	8		Blazar			0.092
44	SWIFT J0550.7−3212	PKS 0548−322	87.6699	−32.2716	y*	7.39	4.4	0.069	44.70	21.50	8		BL Lac		13.59	2.533
45	SWIFT J0552.2−0727	NGC 2110	88.0474	−7.4562	y*	32.46	25.6	0.007789	43.54	22.57	8		Sy 2		9.26	0.010
46	SWIFT J0554.8+4625	MCG +08−11−011	88.7234	46.4393		11.37	11.1	0.020484	44.02	20.30	4		Sy 1.5		10.49	1.689
47	SWIFT J0557.9−3822[l]	EXO 055620−3820.2	89.5083	−38.3346	y*	9.82	5.2	0.03387	44.14	22.23	8	y	Sy 1		11.86	0.105
48	SWIFT J0602.2+2829	IRAS 05589+2828	90.5446	28.4728		5.08	5.6	0.033	44.15	21.57	1		Sy 1			0.866
49	SWIFT J0601.9−8636	ESO 005− G 004	91.4235	−86.6319	y*	5.64	4.2	0.006228	42.56	23.88	1		Sy 2†	43	9.53	
50	SWIFT J0615.8+7101[l]	Mrk 3	93.9015	71.0375	y*	14.27	10.1	0.013509	43.61	24.00	15	y	Sy 2		10.03	0.061
51	SWIFT J0623.9−6058	ESO 121−IG 028	95.9399	−60.9790	y*	4.85	2.8	0.0403	44.03	23.20			Sy 2	44	11.63	0.011
52	SWIFT J0640.4−2554	ESO 490−IG026	100.0487	−25.8954		5.14	3.6	0.0248	43.71	21.48	1		Sy 1.2		11.09	0.273

TABLE 1 — *Continued*

#	*Swift*[a] name	ID[b]	RA[c] deg	Dec[c] deg	$> 15°$ [d]	SNR	$f_{\rm BAT}$ [e]	z	$\log L$ [e] erg s^{-1}	$\log n_H$ cm^{-2}	Ref. [f]	Cmplx [g]	Type [h]	Note [i]	J mag	$f_{\rm ROSAT}$ rate[j,k]
53	SWIFT J0640.1−4328	2MASX J06403799−4321211	100.1583	−43.3558	y	4.51	2.8			23.04	1		Galaxy†	40	14.24	
54	SWIFT J0641.3+3257	2MASX J06411806+3249313	100.3252	32.8254		5.51	5.5	0.047	44.46	22.98	9		Sy 2	45	14.01	
55	SWIFT J0651.9+7426	Mrk 6	103.0510	74.4271	y*	9.55	6.6	0.01881	43.72	23.00	16	y	Sy 1.5		11.07	0.062
56	SWIFT J0742.5+4948	Mrk 79	115.6367	49.8097	y*	7.09	4.7	0.022189	43.72	20.76	13		Sy 1.2		11.19	2.196
57	SWIFT J0746.3+2548	SDSS J074625.87+254902.2	116.6078	25.8173	y*	5.92	4.7	2.9793	48.55	22.00	19		Blazar	19		0.032
58	SWIFT J0759.8−3844	IGR J07597−3842	119.9208	−38.7600		7.79	5.3	0.04	44.29	21.70	1		Sy 1.2			
59	SWIFT J0841.4+7052[l]	[HB89] 0836+710	130.3515	70.8951	y*	11.38	7.0	2.172	48.39	20.98	8		Blazar			0.755
60	SWIFT J0902.0+6007	Mrk 18	135.4933	60.1517	y*	5.35	3.1	0.011088	42.93	23.39	9	y	Galaxy	46	11.50	
61	SWIFT J0904.3+5538	2MASX J09043699+5536025	136.1539	55.6007	y*	5.21	3.4	0.037	44.03	21.89	1		Sy 1		13.55	
62	SWIFT J0911.2+4533	2MASX J09112999+4528060	137.8749	45.4683	y*	5.35	3.0	0.026782	43.69	23.42	1		Sy 2		13.18	
63	SWIFT J0917.2−6221	IRAS 09149−6206	139.0371	−62.3249		4.51	3.2	0.0573	44.40	22.19	1		Sy 1			0.120
64	SWIFT J0918.5+0425	2MASX J09180027+0425066	139.5011	4.4184	y	4.72	3.1	0.156	45.31	23.00	1		QSO 2**	47	14.91	
65	SWIFT J0920.8−0805	MCG −01−24−012	140.1927	−8.0561	y*	6.44	4.6	0.019644	43.60	22.80	14		Sy 2		13.18	
66	SWIFT J0923.7+2255[l]	MCG +04−22−042	140.9292	22.9090	y*	6.38	4.1	0.032349	43.99	20.60	1		Sy 1.2		11.83	1.626
67	SWIFT J0925.0+5218[l]	Mrk 110	141.3036	52.2863	y*	9.26	5.4	0.03529	44.19	20.58	8		Sy 1		13.20	1.691
68	SWIFT J0945.6−1420[l]	NGC 2992	146.4252	−14.3264	y*	9.07	6.6	0.007709	42.94	22.00	20		Sy 2		9.67	0.280
69	SWIFT J0947.6−3057	MCG −05−23−016	146.9173	−30.9489	y*	28.67	21.9	0.008486	43.55	22.47	21		Sy 2		10.53	0.256
70	SWIFT J0959.5−2248[l]	NGC 3081	149.8731	−22.8263	y*	11.34	8.8	0.007956	43.09	23.52	22		Sy 2		9.91	0.008
71	SWIFT J1023.5+1952[l]	NGC 3227	155.8775	19.8650	y*	22.01	12.9	0.003859	42.63	22.80	23	y	Sy 1.5		8.59	0.100
72	SWIFT J1031.7−3451[l]	NGC 3281	157.9670	−34.8537	y*	10.24	7.3	0.010674	43.27	24.30	14	y	Sy 2		9.31	0.012
73	SWIFT J1038.8−4942	2MASX J10384520−4946531	159.6854	−49.7826		4.86	3.3	0.06	44.46	22.17	1		Sy 1†	48	13.24	0.100
74	SWIFT J1040.7−4619	LEDA 093974	160.0939	−46.4238		4.26	3.4	0.023923	43.64	22.96	1		Sy 2		11.44	0.007
75	SWIFT J1049.4+2258	Mrk 417	162.3789	22.9644	y*	6.39	3.6	0.032756	43.95	23.60	9	y	Sy 2		12.74	
76	SWIFT J1104.4+3812[l]	Mrk 421	166.1138	38.2088	y*	14.02	6.8	0.030021	44.15	20.30	25		BL Lac		11.09	16.220
77	SWIFT J1106.5+7234[l]	NGC 3516	166.6979	72.5686	y*	18.26	10.6	0.008836	43.26	21.21	8	y	Sy 1.5		9.74	4.280
78	SWIFT J1127.5+1906	RX J1127.2+1909	171.8178	19.1556	y	4.14	2.2	0.1055	44.79	21.30	1		Sy 1.8	37		
79	SWIFT J1139.0−3743[l]	NGC 3783	174.7572	−37.7386	y*	20.46	16.1	0.00973	43.53	22.47	4	y	Sy 1		9.83	1.130
80	SWIFT J1139.1+5913	SBS 1136+594	174.7873	59.1985	y	4.64	2.5	0.0601	44.33	19.58	1		Sy 1.5		14.83	0.372
81	SWIFT J1143.7+7942	UGC 06728	176.3168	79.6815	y*	5.88	3.7	0.006518	42.54	20.65	9		Sy 1.2		11.62	0.375
82	SWIFT J1145.6−1819	2MASX J11454045−1827149	176.4186	−18.4543	y*	5.26	3.9	0.032949	43.98	20.54	1		Sy 1		13.93	3.293
83	SWIFT J1200.8+0650	CGCG 041−020	180.2413	6.8064	y	4.53	2.5	0.036045	43.88	22.83	1		Sy 2	47	12.15	
84	SWIFT J1200.2−5350	IGR J12026−5349	180.6985	−53.8355		5.37	4.0	0.027966	43.86	22.34			Sy 2		11.48	0.026
85	SWIFT J1203.0+4433	NGC 4051	180.7900	44.5313	y*	9.01	4.6	0.002335	41.74	20.47	8	y	Sy 1.5		8.58	3.918
86	SWIFT J1204.5+2019	ARK 347	181.1237	20.3162	y	4.39	2.3	0.02244	43.42	23.20	1		Sy 2		11.76	0.004
87	SWIFT J1206.2+5243	NGC 4102	181.5963	52.7109	y*	5.00	2.4	0.002823	41.62	20.94	26		Liner		8.76	
88	SWIFT J1209.4+4340[l]	NGC 4138	182.3741	43.6853	y	4.53	2.1	0.002962	41.62	22.90	28		Sy 1.9		9.90	
89	SWIFT J1210.5+3924[l]	NGC 4151	182.6358	39.4057	y*	74.10	37.4	0.003319	42.96	22.48	27	y	Sy 1.5		8.50	0.651
90	SWIFT J1218.5+2952	Mrk 766	184.6105	29.8129	y	4.60	2.3	0.012929	42.94	21.72	8		Sy 1.5		11.10	4.710
91	SWIFT J1225.8+1240[l]	NGC 4388	186.4448	12.6621	y*	45.63	25.3	0.008419	43.60	23.63	4	y	Sy 2		8.98	0.516
92	SWIFT J1202.5+3332	NGC 4395	186.4538	33.5468	y*	5.05	2.6	0.001064	40.81	22.30		y	Sy 1.9		10.66	
93	SWIFT J1229.1+0202[l]	3C 273	187.2779	2.0524	y*	44.58	26.2	0.15834	46.25	20.54	8		Blazar		11.69	7.905
94	SWIFT J1235.6−3954[l]	NGC 4507	188.9026	−39.9093	y*	23.56	19.3	0.011802	43.78	23.46	4	y	Sy 2		9.93	0.032
95	SWIFT J1238.9−2720	ESO 506−G027	189.7275	−27.3078	y*	16.87	13.2	0.025024	44.28	23.60	1	y	Sy 2	48	11.14	
96	SWIFT J1239.3−1611	XSS J12389−1614	189.7763	−16.1799	y*	8.57	5.8	0.036675	44.26	22.48	1		Sy 2	49	11.48	
97	SWIFT J1239.6−0519[l]	NGC 4593	189.9142	−5.3442	y*	14.62	9.1	0.009	43.21	20.30	4	y	Sy 1†		8.96	1.429
98	SWIFT J1241.6−5748	WKK 1263	190.3572	−57.8343		4.09	2.8	0.02443	43.58	21.50	9		Sy 2†		12.29	0.614
99	SWIFT J1256.2−0551	3C 279	194.0465	−5.7893	y*	5.47	3.2	0.5362	46.57	20.41	8		Blazar		19.90	0.400
100	SWIFT J1303.8+5345	SBS 1301+540	195.9978	53.7917	y*	4.82	2.5	0.02988	43.72	20.60	1		Sy 1	50	13.43	0.059
101	SWIFT J1305.4−4928	NGC 4945	196.3645	−49.4682		24.48	19.4	0.001878	42.18	24.60	4		Sy 2†		5.60	0.085
102	SWIFT J1309.2+1139	NGC 4992	197.3040	11.6459	y*	8.45	4.7	0.025137	43.83	23.39	9	y	Galaxy	51	11.23	
103	SWIFT J1322.2−1641[l]	MCG −03−34−064	200.6019	−16.7286	y*	6.53	4.7	0.016541	43.46	23.59	28	y	Sy 1.8		10.80	
104	SWIFT J1325.4−4301[l]	Cen A	201.3650	−43.0192	y*	93.44	74.8	0.001825	42.74	22.74	8	y	Sy 2		4.98	0.411
105	SWIFT J1335.8−3416	MCG −06−30−015	203.9741	−34.2956	y*	9.26	7.5	0.007749	43.00	21.67	8	y	Sy 1.2		10.87	2.496

TABLE 1 — *Continued*

#	*Swift*[a] name	ID[b]	RA[c] deg	Dec[c] deg	$> 15°$ [d]	SNR	$f_{\rm BAT}$ [e]	z	$\log L$ [e] erg s^{-1}	$\log n_H$ cm^{-2}	Ref. [f]	Cmplx [g]	Type [h]	Note [i]	J mag	$f_{\rm ROSAT}$ rate[j,k]
106	SWIFT J1338.2+0433	NGC 5252	204.5665	4.5426	y*	10.52	6.6	0.022975	43.90	25.82	8	y	Sy 1.9		10.89	
107	SWIFT J1347.4−6033	4U 1344−60	206.8500	−60.6400		8.93	7.0	0.012879	45.49	22.37	6		Sy 1.5			
108	SWIFT J1349.3−3018[l]	IC 4329A	207.3304	−30.3096	y*	33.62	30.0	0.016054	44.24	21.65	8		Sy 1.2		10.24	2.960
109	SWIFT J1352.8+6917[l]	Mrk 279	208.2644	69.3082	y*	8.67	4.4	0.030451	43.97	20.53	8		Sy 1.5		11.43	2.809
110	SWIFT J1413.2−0312[l]	NGC 5506	213.3119	−3.2075	y*	30.36	23.6	0.006181	43.30	22.53	4		Sy 1.9		9.71	0.110
111	SWIFT J1417.7+2539	1E 1415+259	214.4862	25.7240	y*	4.92	3.1	0.237	45.71	20.72	1		BL Lac	52		1.710
112	SWIFT J1417.9+2507	NGC 5548	214.4981	25.1368	y*	9.11	5.8	0.01717	43.59	20.41	8	y	Sy 1.5		10.64	4.950
113	SWIFT J1419.0−2639	ESO 511−G030	214.8434	−26.6447	y*	5.73	4.7	0.02239	43.73	21.21	8		Sy 1		10.79	1.221
114	SWIFT J1428.7+4234	1ES 1426+428	217.1361	42.6724	y	4.66	2.6	0.129	45.06	21.52	8		BL Lac			4.200
115	SWIFT J1442.5−1715[l]	NGC 5728	220.5997	−17.2532	y*	8.96	8.9	0.0093	43.23	23.63	17		Sy 2		9.18	
116	SWIFT J1504.2+1025	Mrk 841	226.0050	10.4378	y*	5.56	5.1	0.036422	44.20	21.32	8	y	Sy 1		12.56	0.081
117	SWIFT J1535.9+5751	Mrk 290	233.9682	57.9026	y	4.66	3.0	0.029577	43.79	20.40	8		Sy 1		13.04	0.885
118	SWIFT J1628.1+5145[l]	Mrk 1498	247.0169	51.7754	y*	6.13	4.5	0.0547	44.50	23.26	1		Sy 1.9		12.77	
119	SWIFT J1648.0−3037	2MASX J16481523−3035037	252.0635	−30.5845		6.38	8.6	0.031	44.28	21.61	1		Sy 1		12.56	0.149
120	SWIFT J1652.9+0223	NGC 6240	253.2454	2.4008	y	4.43	4.7	0.02448	43.81	24.34	4		Sy 2		10.30	0.090
121	SWIFT J1654.0+3946	Mrk 501	253.4676	39.7602	y*	7.63	4.9	0.03366	44.11	22.40	8	y	BL Lac		10.67	4.122
122	SWIFT J1717.1−6249	NGC 6300	259.2478	−62.8206		8.76	9.1	0.003699	42.44	23.34	1		Sy 2		7.86	
123	SWIFT J1737.5−2908	GRS 1734−292	264.3512	−29.1800		8.63	10.9	0.0214	44.05	21.96	30		Sy 1			
124	SWIFT J1745.4+2906	1RXS J174538.1+290823	266.4094	29.1395	y*	5.62	3.9	0.111332		20.67	1		Sy 1	45	13.98	0.530
125	SWIFT J1835.0+3240	3C 382	278.7590	32.6973	y*	10.96	8.1	0.05787	44.81	21.13	8		Sy 1		11.87	2.000
126	SWIFT J1838.4−6524[l]	ESO 103−035	279.5847	−65.4276	y*	9.50	9.7	0.013286	43.58	23.17	8		Sy 2		11.38	0.060
127	SWIFT J1842.0+7945[l]	3C 390.3	280.5375	79.7714	y*	17.32	10.1	0.0561	44.88	21.03	8		Sy 1		12.91	0.472
128	SWIFT J1930.5+3414	NVSS J193013+341047	292.5554	34.1797		5.92	3.3	0.0629	44.50	23.20	31		Sy 1	53	14.24	
129	SWIFT J1942.6−1024	NGC 6814	295.6694	−10.3235	y*	5.68	6.2	0.005214	42.57	20.76	32		Sy 1.5		8.66	0.034
130	SWIFT J1952.4+0237	3C 403	298.0658	2.5068		4.29	4.1	0.059	44.53	23.60	33		Sy 2		12.53	
131	SWIFT J1959.4+4044	Cyg A	299.8681	40.7339		16.74	10.9	0.05607	44.91	23.30	26		Sy 2		10.61	0.947
132	SWIFT J1959.6+6507	1ES 1959+650	299.9994	65.1485	y*	6.68	4.1	0.047	44.33	21.11	13		BL Lac		12.54	2.653
133	SWIFT J2009.0−6103	NGC 6860	302.1954	−61.1002	y*	5.08	4.9	0.014884	43.39	21.75	1	y	Sy 1		10.68	0.566
134	SWIFT J2028.5+2543a	MCG +04−48−002	307.1463	25.7336		9.05	6.1	0.0139	43.42	23.60	1	y	Sy 2		11.23	
135	SWIFT J2028.5+2543b	NGC 6921	307.1203	25.7234		9.05	6.1	0.014467	43.45	23.96	3	y	Sy 2		10.01	
136	SWIFT J2042.3+7507[l]	4C +74.26	310.6554	75.1340	y*	8.52	5.0	0.104	45.14	21.25	34	y	Sy 1	54		0.588
137	SWIFT J2044.2−1045[l]	Mrk 509	311.0406	−10.7235	y*	8.36	9.7	0.0344	44.43	20.70	8	y	Sy 1.2		11.58	3.850
138	SWIFT J2052.0−5704[l]	IC 5063	313.0097	−57.0688	y*	7.90	7.1	0.011348	43.31	23.28	8	y	Sy 2		11.10	0.010
139	SWIFT J2114.4+8206	2MASX J21140128+8204483	318.5049	82.0801	y*	5.86	3.6	0.084	44.80	21.11	1		Sy 1†		13.17	0.460
140	SWIFT J2124.6+5057	IGR J21247+5058	321.1589	50.9828		21.74	13.9	0.02	44.10	22.39	1		Sy 1	55		0.026
141	SWIFT J2127.4+5654	IGR J21277+5656	321.9413	56.9429		4.21	2.7	0.0147	43.12	21.98	1		Sy 1	49		0.310
142	SWIFT J2156.1+4728	RX J2135.9+4728	323.9792	47.4731		4.48	2.9	0.025	43.61	21.78	1		Sy 1		12.79	0.124
143	SWIFT J2152.0−3030	PKS 2149−306	327.9812	−30.4650	y*	5.08	5.4	2.345	48.36	20.52	1		Blazar			0.462
144	SWIFT J2200.9+1032	UGC 11871	330.1724	10.5524	y	4.52	3.9	0.026612	43.80	22.21	1		Sy 1.9		11.72	
145	SWIFT J2201.9−3152[l]	NGC 7172	330.5080	−31.8698	y*	12.28	12.4	0.008683	43.32	22.89	8		Sy 2		9.44	0.012
146	SWIFT J2209.4−4711	NGC 7213	332.3177	−47.1667	y*	6.70	5.2	0.005839	42.59	20.60	8	y	Sy 1.5		7.97	3.940
147	SWIFT J2235.9−2602	NGC 7314	338.9426	−26.0502	y*	5.24	5.7	0.00476	42.45	21.79	8	y	Sy 1.9†		9.06	0.236
148	SWIFT J2235.9+3358	NGC 7319	339.0148	33.9757	y*	6.23	4.1	0.022507	43.68	23.38	17	y	Sy 2		11.09	0.001
149	SWIFT J2246.0+3941	3C 452	341.4532	39.6877	y	4.78	3.3	0.0811	44.73	23.43	35		Sy 2		13.35	
150	SWIFT J2253.9+1608	3C 454.3	343.4906	16.1482	y*	21.25	19.0	0.859	47.83	20.77	36		Blazar		14.50	0.263
151	SWIFT J2254.1−1734[l]	MR 2251−178	343.5242	−17.5819	y*	9.53	10.8	0.06398	45.03	20.80	8	y	Sy 1		12.54	1.037
152	SWIFT J2303.3+0852	NGC 7469	345.8151	8.8740	y*	9.35	8.3	0.016317	43.70	20.61	8		Sy 1.2		10.11	1.700
153	SWIFT J2304.8−0843	Mrk 926	346.1811	−8.6857	y*	5.19	5.5	0.04686	44.45	21.14	8		Sy 1.5		11.84	3.530
154	SWIFT J2318.4−4223[l]	NGC 7582	349.5979	−42.3706	y*	10.24	6.7	0.005254	42.61	22.98	8	y	Sy 2		8.35	0.048

TABLE 1 — *Continued*

#	*Swift*[a] name	ID[b]	RA[c] deg	Dec[c] deg	$>15^{\circ}$ [d]	SNR	$f_{\rm BAT}$ [e]	z	$\log L$ [e] erg s^{-1}	$\log n_H$ cm^{-2}	Ref. [f]	Cmplx [g]	Type [h]	Note [i]	J mag	$f_{\rm ROSAT}$ rate[j,k]

REFERENCES. — († † indicates our interpretation of published spectra) : [1] *Swift XRT* [2] *XTE* / Akylas et al. (2002) [3] *XMM* / Winter et al. (2008b) [4] Lutz et al. (2004) [5] Sambruna et al. (1998) [6] *ASCA* / Mushotzky et al. in preparation [7] Gallo et al. (2006) [8] Tartarus database [9] *XMM* / Mushotzky et al. in preparation [10] *EXOSAT* / Mushotzky et al. in preparation [11] Bassani et al. (1999) [12] *ROSAT* / Mushotzky et al. in preparation [13] *XMM* [14] *BeppoSax* [15] Matt et al. (2000) [16] Immler et al. (2003) [17] *Chandra* / Mushotzky et al. in preparation [18] no XRT obvious counterpart [19] Sambruna et al. (2006) [20] Gilli et al. (2000) [21] *RXTE* [22] Maiolino et al. (1998) [23] *XMM* / Gondoin et al. (2003) [24] *BeppoSax* / Vignali, & Comastri (2002) [25] *XMM* / Perlman et al. (2005) [26] *Chandra* [27] Cappi et al. (2006) [28] Risaliti et al. (1999) [29] XRT / *Swift* source/highly absorbed spectrum, no z [30] *ASCA* [31] Kennea et al. (2005) [32] Reynolds (1997) [33] Kraft et al. (2005) [34] Ballantyne (2005) [35] XRT / Evans et al.(2006) [36] *Ginga* / Lawson & Turner (1997) [37] Véron-Cetty & Véron (2001) [38] Lewis, Eracleous & Sambruna (2003) [39] Observed - no AGN lines (Winter et al. 2008a) [40] No spectrum available [41] Schoenmakers et al. (1998) † † [42] 6dF † † [43] Ueda et al. (2007) [44] Donzelli (2000) † † [45] Winter et al. (2008a) [46] Sargent (1970) [47] SDSS † † [48] Morelli et al. (2006) [49] Masetti et al. (2006b) [50] Burenin (2006) [51] SDSS - no AGN lines [52] Giommi et al. (2005) [53] Halpern (2006) [54] Brinkmann et al. (1998) [55] Molina et al. (2006) [56] Bikmaev et al. (2006)

[a] The *Swift* name given is based on the source coordinates from the latest analysis of Swift data except that where a name has been previously published it is kept to avoid confusion.

[b] The ID name given is that of the entry in the NED database (except in those few cases there is none).

[c] J2000 coordinates for the identified counterpart.

[d] 'y' indicates that the source is at $|b| > 15^{\circ}$ and so, if the SNR is also $> 4.8\sigma$ (indicated by 'y*'), is included in the quantitative analysis.

[e] BAT fluxes (in units of 10^{-11} erg cm^{-2} s^{-1}) and luminosities are in the band 14−195 keV. Distances for luminosity were calculated using the measured redshift and assuming it was due to Hubble flow. Luminosity errors must include the error in measured flux and the error in distance due to the random velocity of galaxies (~ 500 km s^{-1}).

[f] Reference for the n_H value - see below.

[g] "cmplx=y" indicates that the spectrum differs significantly from a simple power law with absorption and an Fe line.

[h] This column contains optically derived types. For well studied AGN, the optical type was derived from Véron-Cetty & Véron (2006). For the remaining sources, we determined type by examining the spectrum from archival data or from our own observations. The few remaining AGN without an accessible spectrum are flagged (†).

[i] Reference for the type and/or z, where this is not from NED - see below

[j] *ROSAT* flux in counts s^{-1} from the HEASARC database (Schwope et al., 2000).

[k] The J band is better to use than the K band because it is expected to have a better sensitivity in detecting local AGN. The colors of hard X-ray selected AGN have J/K values ~ 1 at low redshifts, and galaxies at low z also have $J/K \sim 1$ (Watanabe et al 2004). The 2MASS survey is more sensitive in J (http://www.ipac.caltech.edu/2mass/releases/second/doc/figures/secvi2af5.gif), where it is shown that the survey goes ~ 1 mag more sensitive in J than K.

[l] Sources detected in the 3 month survey (Markwardt et al. 2005).

** We classify 2MASX J09180027+0425066 as a QSO because its luminosity is greater than $10^{44.5}$ ergs cm^{-2} s^{-1}, and as type II because of its very strong narrow OIII lines in SSDS.

TABLE 2
COMPARISON OF FITS TO THE AGN LUMINOSITY FUNCTION

Reference $\log L_{14-195}$ (erg s^{-1}) $= 44$	Energy band (keV)	a	b	L_* (ergs s^{-1}) Native band	14−195 keV
This work	14−195	$0.84^{+0.16}_{-0.22}$	$2.55^{+0.43}_{-0.30}$		43.85 ± 0.26
Beckmann et al. (2006b)	20−40	0.80 ± 0.15	2.11 ± 0.22	43.38 ± 0.35	43.99 ± 0.35
Sazonov et al. (2007)	17−60	$0.76^{+0.18}_{-0.20}$	$2.28^{+0.28}_{-0.22}$	43.40 ± 0.28	43.74 ± 0.28
Barger et al. (2005)	2−8	0.42 ± 0.06	2.2 ± 0.5	44.11 ± 0.08	44.54 ± 0.08
La Franca et al. (2005)	2−10	$0.97^{+0.08}_{-0.10}$	$2.36^{+0.13}_{-0.11}$	44.25 ± 0.18	44.61 ± 0.18
Sazonov and Revnivtsev (2004)	3−20	$0.88^{+0.18}_{-0.20}$	$2.24^{+0.22}_{-0.18}$	$43.58^{+0.32}_{-0.30}$	$43.83^{+0.32}_{-0.30}$

NOTE. — Luminosities have been converted to 14−195 keV values assuming a low energy slope of 1.7 breaking to 2.0 at 10 keV. Uncertainties do not take into account the uncertainty in the conversion. La Franca et al. quote a range of solutions; a representative one is used here.
The normalization of the BAT AGN luminosity function (A) is $1.8^{+2.7}_{-1.1} \times 10^{-5}$ erg s^{-1} Mpc^{-3} at $\log L$(erg s^{-1})$= 44$.